ACS APPLIED MATERIALS & INTERFACES

www.acsami.org

Research Article

Self-Assembled Chromogenic Polymeric Nanoparticle-Laden Nanocarrier as a Signal Carrier for Derivative Binary Responsive Virus Detection

Indra Memdi Khoris, Akhilesh Babu Ganganboina, and Enoch Y. Park*

Cite This: *ACS Appl. Mater. Interfaces* 2021, 13, 36868−36879

Read Online

ACCESS | Metrics & More | Article Recommendations | Supporting Information

ABSTRACT: In the current biosensor, the signal generation is limited to single virus detection in the reaction chamber. An adaptive strategy is required to enable the recognition of multiple viruses for diagnostics and surveillance. In this work, a nanocarrier is deployed to bring specific signal amplification into the biosensor, depending on the target viruses. The nanocarrier is designed using pH-sensitive polymeric nanoparticle-laden nanocarriers (PNLNs) prepared by sequential nanoprecipitation. The nanoprecipitation of two chromogens, phenolphthalein (PP) and thymolphthalein (TP), is investigated in three different solvent systems in which PNLNs demonstrate a high loading of the chromogen up to 59.75% in dimethylformamide (DMF)/dimethyl sulfoxide (DMSO)/ethanol attributing to the coprecipitation degree of the chromogens and the polymer. The PP-encapsulated PNLNs (PP@PNLNs) and TP-encapsulated PNLNs (TP@PNLNs) are conjugated to antibodies specific to target viruses, influenza virus A subtype H1N1 (IV/A/H1N1) and H3N2 (IV/A/H3N2), respectively. After the addition of anti-IV/A antibody-conjugated magnetic nanoparticles (MNPs) and magnetic separation, the enriched PNLNs/virus/MNPs sandwich structure is treated in an alkaline solution. It demonstrates a synergy reaction in which the degradation of the polymeric boundary and the pH-induced colorimetric development of the chromogen occurred. The derivative binary biosensor shows feasible detection on IV/A with excellent specificities of PP@PNLNs on IV/A/H1N1 and TP@PNLNs on IV/A/H3N2 with LODs of 27.56 and 28.38 fg mL^{-1}, respectively. It intrigues the distinguished analytical signal in human serum with a variance coefficient of 25.8% and a recovery of 93.6−110.6% for one-step subtype influenza virus detection.

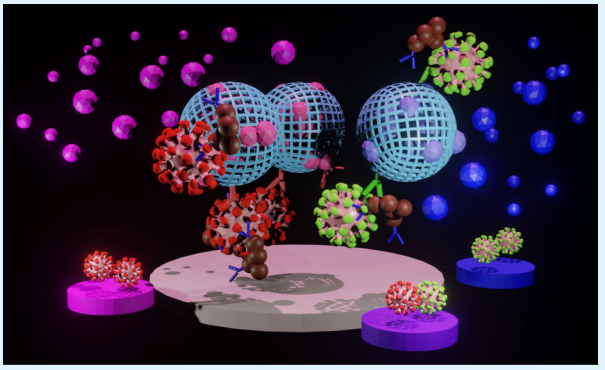

KEYWORDS: *nanoprecipitation, polymeric nanocarrier, influenza virus, derivative spectra, binary biosensor, colorimetric detection*

INTRODUCTION

In the past decade, the worldwide society has been stomped upon the outbreak of an infectious disease-causing virus, including the recent pandemic of SARS-CoV-2,[1] rapid and annual influenza virus,[2] and deadly mosquito-borne viruses.[3] The breakthrough effort in monitoring the viral outbreak has led to the innovation and growth of nanobiosensors.[4−6] During the increasing cases of SARS-CoV-2 infection, the challenge of the global circulating influenza virus with influenza virus type A subtype H1N1 (IV/A/H1N1) and subtype H3N2 (IV/A/H3N2) as the major subtypes can be considered a deadly issue for its worldwide outbreak and sporadic infection with similar spatial and timeline periods.[7] Also, starting from 2011[8] to recently,[9] similar to an antibiotic, an emerging contagious mutant strain on several subtypes of influenza viruses has been a new concern for fighting this "old and persistent" respiratory virus. These worldwide issues have been picturizing the need of the society for prevention action and surveillance technology.[10] Hence, a new approach to virus detection is required to countermeasure the rapidly mutating influenza virus in the early stage for better surveillance and appropriate medical treatment.

An immunoassay[11−13] and a nucleic acid-based biosensor[14−16] are the majorly developed platforms for virus detection. Nucleic acid-based detection provides higher sensitivity but with the cost of complexity and resources.[17,18] On the other hand, the immunoassay implies its simplicity and mobility; still, it suffers from low sensitivity detection due to the limitation on the amplification of the analytical signal.[19,20] In addition, the available platforms are constrained to single

Received: May 12, 2021
Accepted: July 20, 2021
Published: July 30, 2021

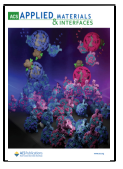

target detection due to their signal generation mechanism.[21] Recently, Zhu *et al.* demonstrated a microfluidic electrochemical sensor with multiple enzymes to monitor the biomarkers in leukemia tumors.[22] The method is based on the metabolite change in the sample and interaction with the multiple enzymes. However, multiple enzymes are limited in terms of colorimetric signal and their vulnerability to a physical condition that affects the biosensors' performance. Instead of relying on an enzyme−substrate chromogenic mechanism, the group of chromogens should be responsive to a single stimulus, and each chromogen exhibits a unique signal, such as a pH-sensitive indicator substrate.[23] The chromogen-dependent biosensor can bridge the transition from the single signal to the multiple response biosensor. Associating the multiple responses in a single readout translates more details on the viruses in the sample.

To integrate the multiple responses and high signal generation, the abundant chromogens should be introduced in the biosensor. A nanocarrier has shown the integration of substrate encapsulation and signal enrichment. Several published nanocarriers, such as the hydrophobic interaction of curcumin on MoS_2[24] and π-stacking interaction of thymolphthalein and metal−organic framework-polydopamine,[25] both as signal molecule nanocarriers, show a high loading capacity and efficiency.[26] Taking an example of a previous nanocarrier-based immunoassay, Yan *et al.*[27] demonstrated dye-encapsulated ZIF-8 for colorimetric biosensing. However, the ZIF nanocarrier has a slight drawback due to the leakage of free signal molecules from the nanocarrier due to the loosened binding.[28] Also, the reaction time in the sensing is considered slow because of the slow molecule-releasing mechanism.

On the other hand, recently, the progress on nanoprecipitation underlines the importance of the solvent composition to the degree of co-nanoprecipitation.[29] Xu *et al.*[30] demonstrated organic dye nanoprecipitation by protein nanocarriers and substrate crystallization. The all-in-one nanoprecipitation shows high substrate precipitation but quite random substrate nanoprecipitation and antibody orientation, leading to a lower immunoassay efficiency. The substrate encapsulation content of protein co-nanoprecipitation is estimated to be as low as <10% due to the protein's limited hydrophobic sites.[26] In another study, Wu *et al.* demonstrated high loading of the fluorescent dye in the presence of polymeric nanoparticles using various solvents and their mixture.[31] The finding establishes that the nanoprecipitation can be engineered to achieve higher content loading by adjusting the solubilities of the substrate and the polymer. The substrate should precipitate initially, followed by polymer precipitation. An organic solvent, such as dimethylformamide (DMF) and dimethyl sulfoxide (DMSO), has been considered as a suitable solvent for the organic substrate with slightly different dielectric constant and viscosities.[32] In addition, ethanol is regarded as a non-good solvent to an organic substrate and has higher permeability to water, which is used as an antisolvent in nanoprecipitation.[33] Hence, solvent selection and its mixture are essential in sequential nanoprecipitation, which presents the new chapter to high-loading nanocarriers.

Here, the polymeric nanoparticle-laden nanocarriers (PNLNs) are prepared by polymeric nanoprecipitation in the copresence of the pH-sensitive chromogen, establishing a pH-responsive colorimetric biosensing platform. The PNLNs are prepared by the precipitation of chromogens, like phenolphthalein (PP) and thymolphthalein (TP), which form PP@PNLNs and TP@PNLNs. By conjugating the PNLNs and magnetic nanoparticles (MNPs) to corresponding antibodies specific to subtypes of influenza viruses, the PNLN-based biosensor is coupled to magnetic separation. The conjugated specific antibodies to subtypes IV/A/H1N1 and IV/A/H3N2 on the PP@PNLNs and TP@PNLNs, respectively, cause the biosensor to be selective to IV/A and its subtype specifically. The specific PNLNs form sandwich structures to IV/A and magnetic nanoparticles (MNPs). Alkaline treatment of the separated PNLNs/virus/MNPs will simultaneously lyse the polymeric boundary of PNLNs, and the chromogen indicator will generate its conjugate base, showing a colorimetric signal depending on the bound PNLNs on the viruses (Scheme S1). The analysis of the binary response shows an intrinsic pattern of virus detection. The signal invigorates the subtype of IV/A in discrete peaks by the derivative analysis of the binary response. Following the signal's elevation, the concentration of the bound viruses can be estimated in a single readout using the PNLN-based biosensor. By adopting this one-pot platform, these results are expected to contribute insight into developing a versatile and straightforward diagnostic biosensor for the corresponding subtypes of viruses in colorimetric detection.

EXPERIMENTAL METHODS

Chemicals and Biological Agents. Dimethyl sulfoxide (DMSO) was purchased from Dojindo (Osaka, Japan). Phenolphthalein (PP), thymolphthalein (TP), bovine serum album (BSA), dimethylformamide (DMF), and dialysis cellulose membrane were purchased from Wako Pure Chem Inc. (Osaka, Japan). Ethanol (99%), the Amicon ultracentrifugation tube, poly(D,L-lactide-*co*-glycolide) acid terminated (PLGA), *N*-hydroxysuccinimide (NHS), and *N*-(3-dimethylaminopropyl)-*N*′-ethylcarbodiimide hydrochloride (EDC) were obtained from Sigma-Aldrich Co. (St. Louis, MO, USA). The various subtypes of influenza viruses were purchased from ProSpec-Tany Technogene, Ltd. (East Brunswick, NJ, USA).

Anti-IV/A/H1, H2, and H3 (Anti-HA), anti-IV/A/H1N1, and anti-IV/A/H3N2 antibodies were purchased from Sino Biological Inc. (Beijing, China). Hepatitis E virus-like particles (HEV-LPs) expressed by the baculovirus expression system were provided by Dr. Tian Chen Li from the National Institute of Infectious Disease, Japan. The norovirus-like particle (NoV-LP) was expressed using a baculovirus expression system.[34] All experiments were conducted using deionized (DI) water.

Preparation of Polymeric Nanoparticle-Laden Nanocarriers (PNLNs), PP@PNLNs, and TP@PNLNs. PP@PNLNs were prepared using the sequential nanoprecipitation method. Four milligrams of PP and 10 mg of PLGA were added into a trisolvent mixture of DMF/DMSO/ethanol (4:4:2, v/v/v). This mixture is defined as a solvent of high solubility to the chromogen and polymer. Then, phosphate-buffered saline (PBS, pH 7.2) acted as an antisolvent, which is a poor constituent that promotes precipitation of the chromogen/polymer instead of dissolving the substance, and was added to the mixture, and PP and PLGA were coprecipitated, forming PP@PNLNs. The PNLNs were further diluted to lower the organic solvent percentage and centrifuged using an Amicon filter of 30 kDa cutoff (Millipore, Germany) to remove excess chromogens from the solution, followed by slow centrifugation to remove large aggregates. To synthesize TP@PNLNs, TP was used instead of PP using a similar method.

Preparation of Amine-Functionalized Magnetic Nanoparticles (A-MNPs). Briefly,[35] $FeCl_3{\cdot}6H_2O$ (0.33 g) was dissolved in EG (10 mL) to form a clear solution, followed by the addition of potassium acetate (0.78 g) and 1,6-hexanediamine (2.2 g). The mixture was stirred vigorously for 30 min and transferred into a Teflon-lined autoclave. The autoclave was heated to and maintained

https://doi.org/10.1021/acsami.1c08813
ACS Appl. Mater. Interfaces 2021, 13, 36868−36879

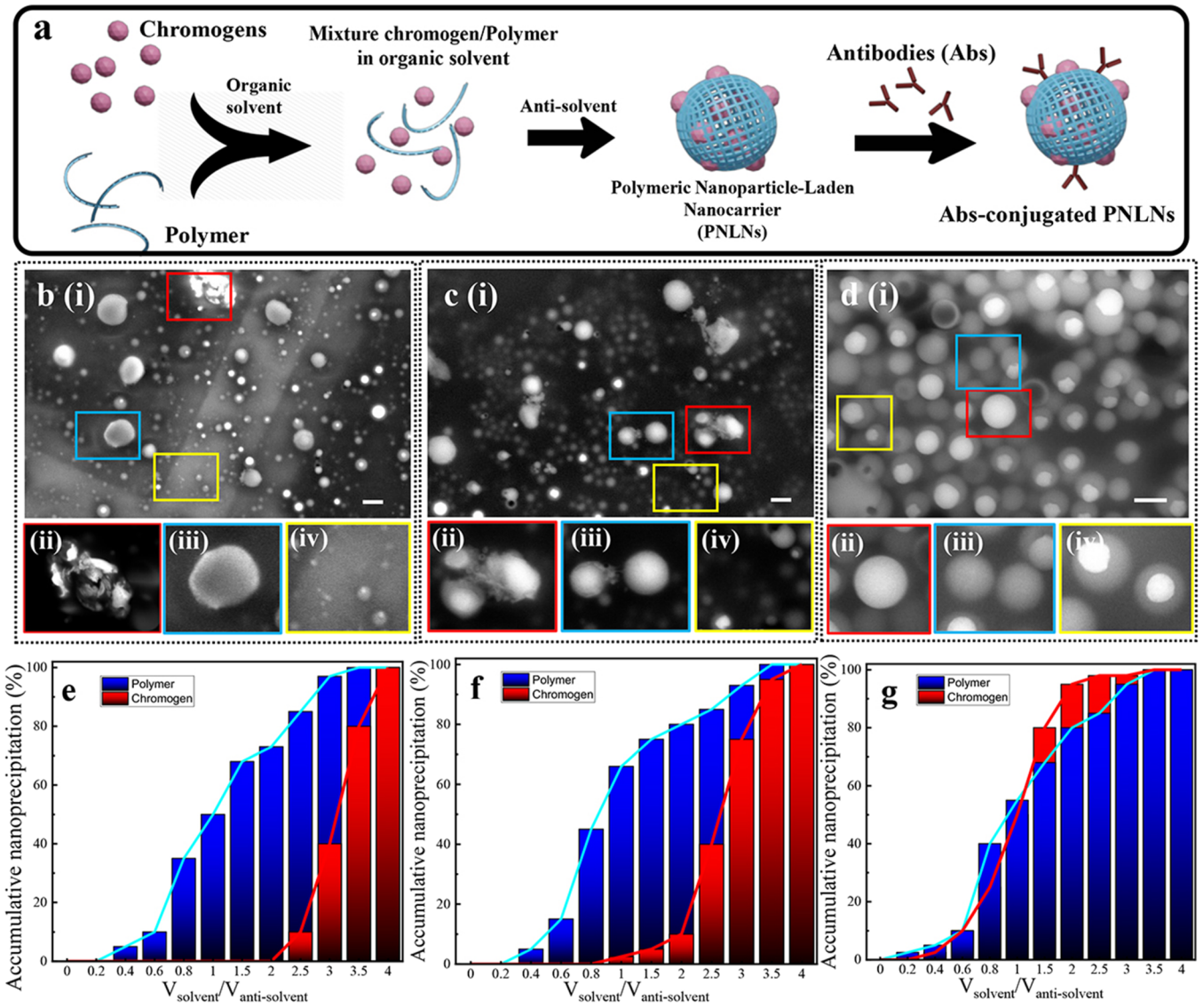

Figure 1. Morphology of the PNLNs prepared using nanoprecipitation in a solvent mixture system. (a) Schematic illustration of PNLN preparation for immunoassay purpose. SEM images of PNLNs in (b) one-solvent, (c) two-solvent, and (d) three-solvent systems (scale bar: 1 μm) (ii–iv represent the magnification of the SEM image). The nanoprecipitation percentage of the polymer and the dye in (e) one-solvent, (f) two-solvent, and (g) three-solvent systems.

at 180 °C for 10 h. The black products were rinsed using ethanol/water.

Characterizations. Scanning electron microscopy (SEM) images were obtained using a scanning electron microscope (JSM-6510LV, JEOL, Japan). Transmission electron microscopy (TEM, JEM-2100F, JEOL, Ltd., Japan) and Fourier transform infrared (FT-IR) spectroscopy analysis were conducted with an FT-IR 6300 (JASCO, Tokyo, Japan). The UV–Vis absorption spectra were measured using a UV-1800 (Shimadzu, Kyoto, Japan).

Colorimetric Analysis of the pH-Sensitive PNLNs. The colorimetric analysis was conducted by reacting the PNLNs with an alkaline solution containing 1 M NaOH. The absorbance spectra were scanned from 400 to 700 nm.

Preparation of Antibody-Conjugated A-MNPs, PP@PNLNs, and TP@PNLNs. The anti-IV/A/HA, anti-IV/A/H1N1, and anti-IV/A/H3N2 antibodies were conjugated to A-MNPs, PP@PNLNs, and TP@PNLNs, respectively, using EDC/NHS carbodiimide conjugation as described in our previous work.[36] EDC/NHS carbodiimide chemistry conjugation activates the carboxylic group of the polymeric PLGA membrane of the PNLNs and reacts to the amine group on the antibodies. The EDC/NHS chemistry results in the amide bond between the PNLNs and the antibodies. As A-MNPs lack a carboxylic group, A-MNPs are initially reacted with succinic anhydride, converting the primary amine group on the surface of the A-MNPs into the carboxylic group by forming an amide bond. The COOH-MNPs are magnetically purified from excess succinic anhydride. Then, the carboxylic group is first activated with EDC and magnetically separated to remove excess EDC reagent. Then, NHS and antibodies are added into the EDC-activated MNPs to form the amide bond with the amine group of the antibodies. The antibody-conjugated PP@PNLNs and TP@PNLNs were purified by mild centrifugation and antibody-conjugated magnetic nanoparticles (Ab-MNPs) by magnetic separation and kept in PBS buffer. Blocking of the free surface of Ab-MNPs was carried out using 2% BSA.

Detection of IV/A/HINI and IV/A/H3N2 and Subtype Detection. Briefly, IV/A was prepared in dilution concentration from the nanogram level to the femtogram level. For IV/A/H1N1 detection, each vial containing the virus was added with 50 μL of Ab-MNPs and 50 μL of Ab-PP@PNLNs and mixed for 2 min by pipetting motion, followed by 20 min incubation time to form the sandwich structure between Ab-MNPs, IV/A, and Ab-PP@PLGA PNLNs. Afterward, the unbound Ab-PP@PNLNs in the supernatant

https://doi.org/10.1021/acsami.1c08813
ACS Appl. Mater. Interfaces 2021, 13, 36868–36879

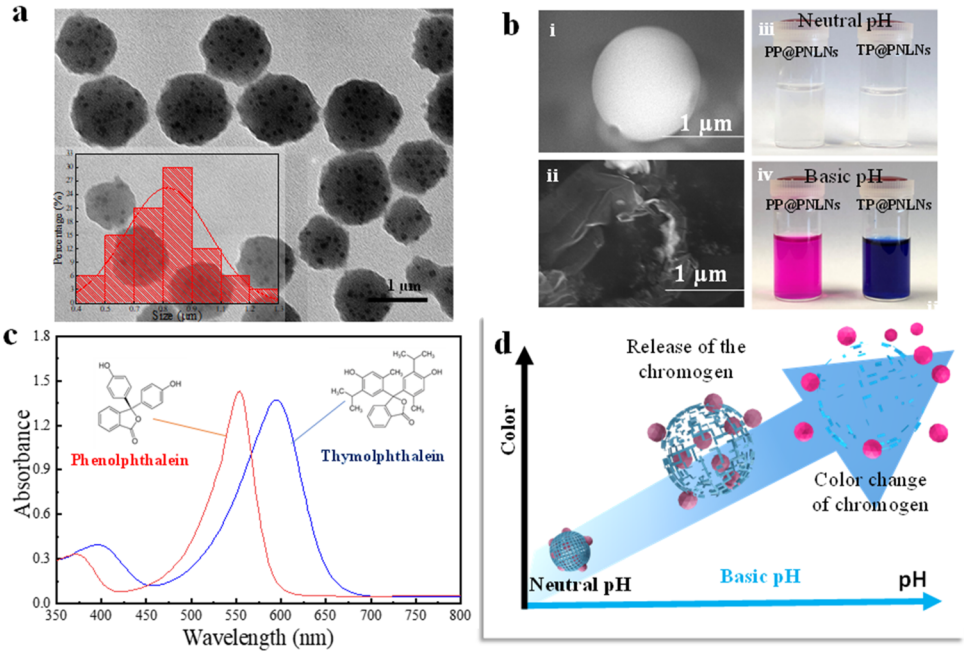

Figure 2. Characterization of PNLNs and the release of the chromogen from the PNLNs; (a) TEM image of PP@PNLNs (inset: size distribution of the PP@PNLNs); (b) SEM images (i and ii) of PNLNs and digital images of the solution color in neutral pH (top) and alkaline pH (bottom); (c) absorbance spectra of pH-sensitive chromogen, phenolphthalein, and thymolphthalein; (d) schematic illustration of the alkaline treatment as the release mechanism of PNLNs.

were removed by magnetic separation, and the washing step was done with PBS buffer. To exhibit the colorimetric detection, the redispersed sandwich structure Ab-MNPs/(IV/A)/Ab-PP@PNLNs was reacted with alkaline solution. The developed color was measured with a UV−Vis microplate reader. For IV/A/H3N2 detection, Ab-TP@PNLNs were added into the virus solution instead of Ab-PP@PNLNs. Further, Ab-PP@PNLNs and Ab-TP@PNLNs (1:1, v/v) were co-added into the virus solution to perform one-pot subtype IV/A detection.

RESULTS AND DISCUSSION

Synthesis and Characterization of PNLNs. Taking advantage of the rapid nanoprecipitation method, the PNLNs are formed by the coprecipitation of the chromogenic dye and polymer, as shown in Figure 1a. Initially, to optimize the solvent mixture for nanoprecipitation, the chromogens, PP or TP, and poly-(lactic-*co*-glycolic acid) (PLGA) were dissolved in a one-solvent system (DMF), two-solvent system (DMF/DMSO), and three-solvent system (DMF/DMSO/ethanol). Further, phosphate-buffered saline (PBS, pH 7.2) as an antisolvent was added to induce the coprecipitation of the chromogen and the polymer. The ratios of 1:1 (v/v) DMF/DMSO for the two-solvent system and 2:2:1 (v/v/v) DMF/DMSO/EtOH for the three-solvent system are obtained based on the derived count rate of the PLGA polymer nanoprecipitation. The morphology of the PNLNs was investigated by scanning electron microscopy. The PNLNs are prepared using a one-solvent system (DMF) (Figure 1b-i) and show various sizes and shapes obtained from the observable aggregation (Figure 1b-ii), moderate nanoparticles (Figure 1b-iii), and smaller size of nanoprecipitation (Figure 1b-iv).

Next, the same ratio of the chromogen and polymer was prepared using a two-solvent system (DMF/DMSO), which is seen to form spherical-like structure PNLNs in general (Figure 1c-i). The smooth and round PNLNs are observed having a uniform size together with several dye aggregates attached on the surface of the PNLNs (Figure 1c-ii,iii). Still, several sporadic chromogen aggregations, which are not bound to the PNLNs, are observed with relatively small sizes (Figure 1c-iv). Attributing to the three-solvent system (DMF/DMSO/ethanol), the uniform and defined morphology of PNLNs is shown in Figure 1d, in which neither random chromogen aggregates nor chromogen precipitation formed on the surface of the PNLNs is observed, showing that a mixture of DMF/DMSO/ethanol can demonstrate desired nanoprecipitation of the PNLNs.

To understand the formation of the morphology of the PNLNs in the solvent system, the scattering intensity of dynamic light scattering (DLS) on individual components, chromogen, and polymer in the solvent mixture was measured.[37−39] The nanoprecipitation percentage is based on the attenuation and count intensity of the scattering light as a function of volume ratio of solvent/antisolvent ($V_{solvent}/V_{antisolvent}$). In the one-solvent system, there is an indication of a gap between the precipitation timeline between the chromogen and the polymer (Figure 1e). At a low volume of antisolvent, the chromogen is in soluble form and remains in the organic solvent. However, the polymer has started emulsifying, stabilizing the surface turbulence between the solvents. Along with the addition of the antisolvent, the nucleus growth of the chromogen nanoprecipitation is gradually observed. It stipulates that the polymer precipitates before the precipitation of the chromogen. While the chromogen is precipitating, the polymer NPs might have been completely established, forming particles and leading to aggregation of the chromogen. In Figure 1f, the two-solvent system shows 50% lower $V_{solvent}/V_{antisolvent}$ required than the one-solvent system for the chromogen to initiate the precipitation. Still, both systems indicate the precipitation of the polymer starting at $V_{solvent}/V_{antisolvent}$ as low as 0.4. By partial substitution of DMSO in a two-solvent system, the

https://doi.org/10.1021/acsami.1c08813
ACS Appl. Mater. Interfaces 2021, 13, 36868−36879

chromogen demonstrated favorable precipitation in low $V_{antisolvent}$, and the coprecipitation of the polymer and chromogen can occur. This drives the growth of the chromogen nanoparticles on the polymeric membrane instead of forming self-aggregating colloids. In addition, the three-solvent system involves ethanol in the mixture of DMSO and DMF. As shown in Figure 1g, low $V_{antisolvent}$ can engage rapid precipitation of the chromogen due to the miscibility of ethanol to the antisolvent like PBS. These results in higher coprecipitation of the chromogen and the polymer, forming the PNLNs. The coprecipitation has also resulted in a bigger size of the PNLNs included in the system. In the extensive study, introducing the high amount of chromogen in the three-solvent mixture will also result in the aggregation of the chromogen on the surface of the PNLNs (Figure S1).

The variation of nanoprecipitation using a multiple solvent mixture system can be attributed to several factors: (1) The solubility of the chromogen PP is indicated by the nanoprecipitation of the PP in the one-solvent system as a function of PP concentration (Figure S2). DMF (Figure S2a) and DMSO (Figure S2b) result in bigger PP nanoparticle size (black circles) compared to ethanol (Figure S2c) as a solvent. Still, they indicate a lower polydispersity index (PDI) (red circles of Figure S2) than in ethanol. A higher PDI (>0.3) means bigger instability and heterogeneous nucleation in the system. In high concentrations of PP, DLS analysis in DMF and DMSO shows the large hydrodynamic size, indicating the formation of bigger size particles from the nanoprecipitation. (2) Compared to DMSO and DMF, ethanol has higher dielectric properties with less viscosity and is more miscible to water. (3) There is optimum particle formation from the PLGA nanoprecipitation in the three-solvent system than in the one-solvent system or two-solvent system.

Further, the encapsulation of the chromogens in the PNLNs is investigated by DLS analysis and TEM analysis of PP@PNLNs. As shown in Figure 2a, PP@PNLNs have spherical PNLNs with several black dots within the PNLNs. The size of the PNLNs is estimated at around 0.9 μm, which is in agreement with the hydrodynamic size of the PP@PNLNs around 964.65 ± 123.25 nm with a PDI value of 0.226, and the smaller spherical black dots are estimated around 50−100 nm. There are no observable chromogen aggregates, indicating the higher degree of encapsulation of the chromogen within the polymeric boundary. Similarly, the synthesized TP@PNLNs show a spherical shape with a size of 0.85 μm (Figure S3). The formation of the PP@PNLNs and TP@PNLNs is caused by the chemistry interaction between the polymer and the chromogens, PP and TP. Both chromogens are built up by mostly hydrocarbons and several hydroxyl groups, and this results in their poor solubility to an aqueous phase and good solubility to an organic solvent and ethanol, like the PLGA polymer. Most likely, the PLGA and chromogens showcase hydrophobic interaction and hydrogen bonding via the hydroxyl group of the PP and TP and the carbonyl group of the PLGA.[40,41]

The Release Mechanism of the Chromogen@PNLNs. The chromogen loading calculation is based on the calibration curve of PP in solution (pH 10) (Figure S4). The calibration curve of PP is obtained from the absorbance at 550 nm as a function of PP concentration. The PP@PNLNs are weighted, and the absorbance of the PP@PNLNs in pH 10 solution is measured. The encapsulation efficiencies of the PP@PNLNs using one-solvent, two-solvent, and three-solvent mixtures were estimated around 29.02, 32.44, and 53.15%, respectively. Compared to their counterpart of one-solvent and two-solvent systems, by using three-solvent combinations, the nanoprecipitation demonstrates the PNLNs with higher chromogen coprecipitation inside the polymeric boundary. Further, the loading capacities of the PP@PNLNs and TP@PNLNs are 11.33% (w/w) and 15.4% (w/w), respectively. The loading capacity is measured based on the chromogen loaded in the polymer over the weight of the PNLNs. The chromogen molecules per PNLN are calculated around 2.22×10^4 PP molecules per NP and 1.41×10^4 molecules per NP based on the hydrodynamic size of the PNLNs (V_{NP}) and the molar volume of the chromogens ($V_{Chromogen}$).[42,43]

PNLNs were encapsulated in pH-sensitive chromogens, PP and TP, which will show color development in basic pH conditions. The PNLNs are investigated in the basic pH to understand its stability. The PNLN-encapsulating chromogens, PP and TP, were observed by the SEM image analysis. Under the scanning electron microscope, the smooth spherical structure of the PNLNs is observed (Figure 2b-i). However, upon an alkaline treatment, as shown in Figure 2b-ii, the PNLNs are ruptured and indicate no observable spherical structure. This indicates that the polymer boundary of PNLNs is lysis in the basic pH environment in which PLGA is known to undergo alkaline hydrolysis to lactic acid and glycolic acid.[44,45] As the polymeric boundary is removed, the chromogens are released and are stimulated in the basic pH environment, developing a color change. Initially, the PNLN solution is colorless in neutral pH, as shown in Figure 2b-iii. Upon the alkaline treatment, the PP-encapsulating PNLNs (PP@PNLNs) turn to a pinkish color, and TP-encapsulating PNLNs (TP@PNLNs) turn to a bluish color (Figure 2b-iv). The alkaline-triggered developed color from PP@PNLNs and TP@PNLNs shows single peak absorbance color at 560 and 590 nm (Figure 2c). Accordingly, the alkaline treatment on the pH-sensitive PNLNs can break down the polymeric membrane and expose the chromogen to the basic pH condition. The colorimetric signal pivots on the dual response of the lysis of the PNLNs and the pH-sensitive chromogens in the alkaline environment (Figure 2d).

To be applied in the virus biosensing, the nanocarriers, PNLNs, and magnetic nanoparticles (MNPs) are required to be conjugated with specific antibodies against the target virus IV/A. As shown in Figure S5, ELISA results show higher absorbance in antibody-conjugated PNLNs (Ab-PNLNs) and MNPs (Ab-MNPs) than those in only PNLNs and MNPs, respectively. Free antibodies and 2% BSA are used as the positive control and negative control, respectively, in ELISA. To understand the advantage of the higher loading capacity of the nanocarriers in biosensing purposes, a comparative study is conducted on the IV/A/H1N1 detection using one-solvent mixture-prepared PP@PNLNs (PP@1PNLNs), two-solvent mixture-prepared PP@PNLNs (PP@2PNLNs), and three-solvent mixture-prepared PP@PNLNs (PP@3PNLNs). Three kinds of Ab-PP@PNLNs are assayed to the immobilized IV/A/H1N1 solution on the 96-well microplate. After IV/A/H1N1 was added to the antibody-conjugated PP@PNLNs (Ab-PP@PNLNs), the well was rinsed to remove unbound Ab-PP@PNLNs. The bound Ab-PP@PNLNs were alkaline-treated, and the developed color was measured. Figure S6 indicates that the Ab-PP@1PNLNs-based biosensor demonstrated the lowest detection signal, followed by Ab-PP@2PNLNs and Ab-PP@3PNLNs, which generate the highest

https://doi.org/10.1021/acsami.1c08813
ACS Appl. Mater. Interfaces 2021, 13, 36868−36879

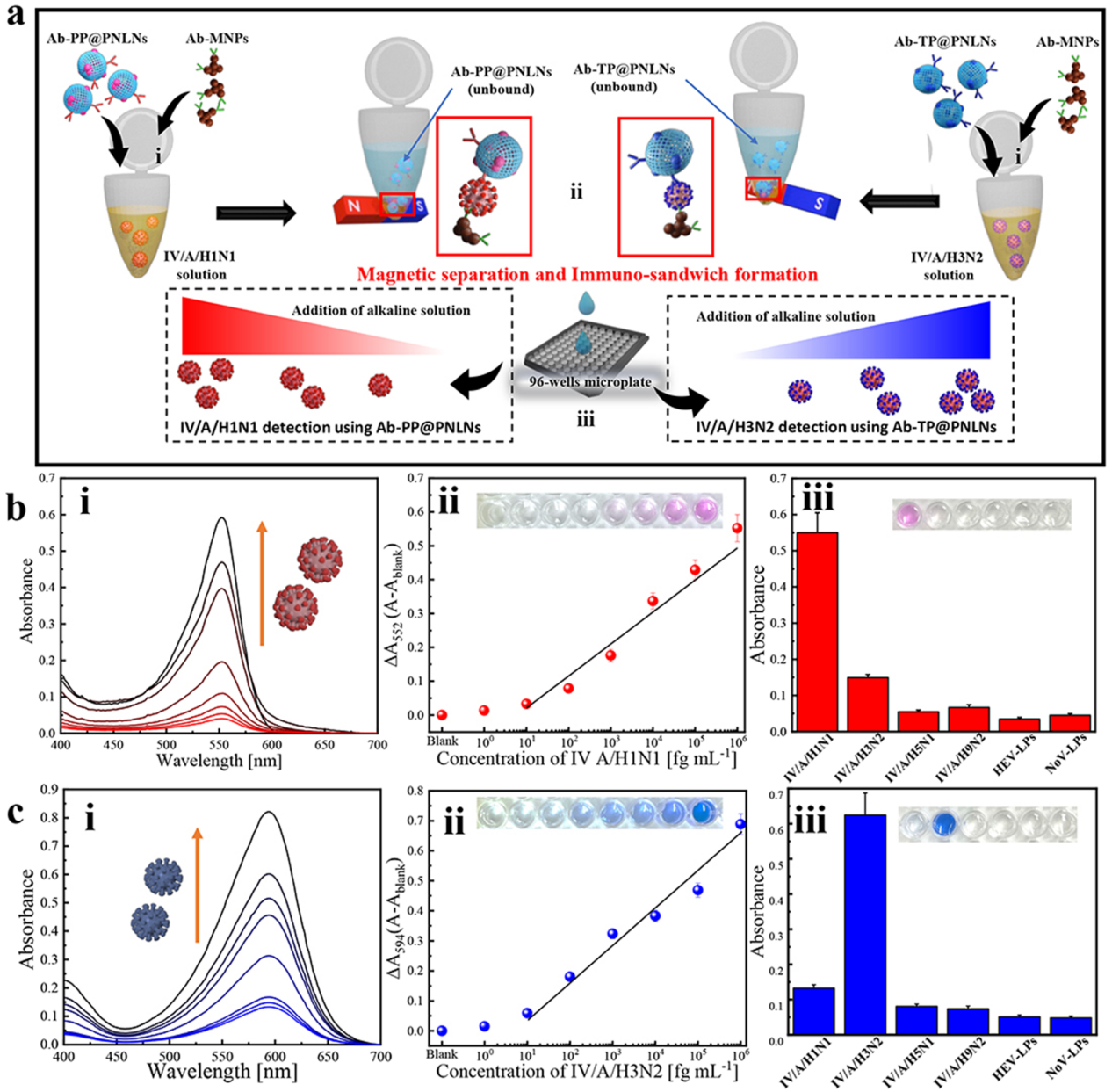

Figure 3. IV/A detection using the PNLN-based biosensor. (a) Schematic illustration of the PNLN-based biosensor: (i) addition of Ab-MNPs and Ab-PNLNs into the virus solution, (ii) magnetic separation and immunosandwich complex formation, and (iii) alkaline treatment for colorimetric detection. Panels (b) and (c) show IV/A/H1N1 and IV/A/H3N2 detections using PP@PNLNs- and TP@PNLNs-based biosensors, respectively. (b, c) (i) Absorbance spectra of the detection result, (ii) absorbance plotting in the function of IV/A concentration, and (iii) selectivity test of the corresponding PNLN-based biosensor. The inset images show the developed color taken by a digital camera.

signal. Three of the PNLNs show a negligible signal in the absence of IV/A/H1N1. This highlights that the three-solvent mixture-prepared PNLNs, which have the highest loading of the chromogen, also provide the highest signal amplification in the virus detection, implicating the fundamental advancement in the nanocarrier-based biosensor.

The magnetic separation is used to remove excessive nontarget matrix components in the detection sample and reduce the background noise.[46] Amine-functionalized magnetic nanoparticles (A-MNPs) are used for separating the PNLNs bound to the influenza virus (IV/A) by a magnetic field. A-MNPs are shown to be spherical with a size around 50 nm, as shown in Figure S7a. The functional group analysis using FT-IR analysis shows the peak at 3427 cm^{-1} (Figure S7b), indicating an amine functionalization.

Analytical Performance of the PNLN-Based Biosensor for Influenza Virus and Its Specificity. Antibody-conjugated A-MNPs (Ab-MNPs), antibody-conjugated PP@PNLNs (Ab-PP@PNLNs), and TP@PNLNs (Ab-TP@PNLNs) were introduced into the system to separate and detect IV/A. As the capturing probe, A-MNPs were conjugated to antibodies specific to H1, H2, and H3. PP@PNLNs and TP@PNLNs were conjugated to antibodies specific to H1N1 and H3N2, respectively. Ab-MNPs and Ab-PP@PNLNs or Ab-TP@PNLNs will bring the substrate along with the binding virus for signal generation. As shown in Figure 3a, Ab-MNPs, Ab-PP@PNLNs, and Ab-TP@PNLNs were introduced to the

https://doi.org/10.1021/acsami.1c08813
ACS Appl. Mater. Interfaces 2021, 13, 36868−36879

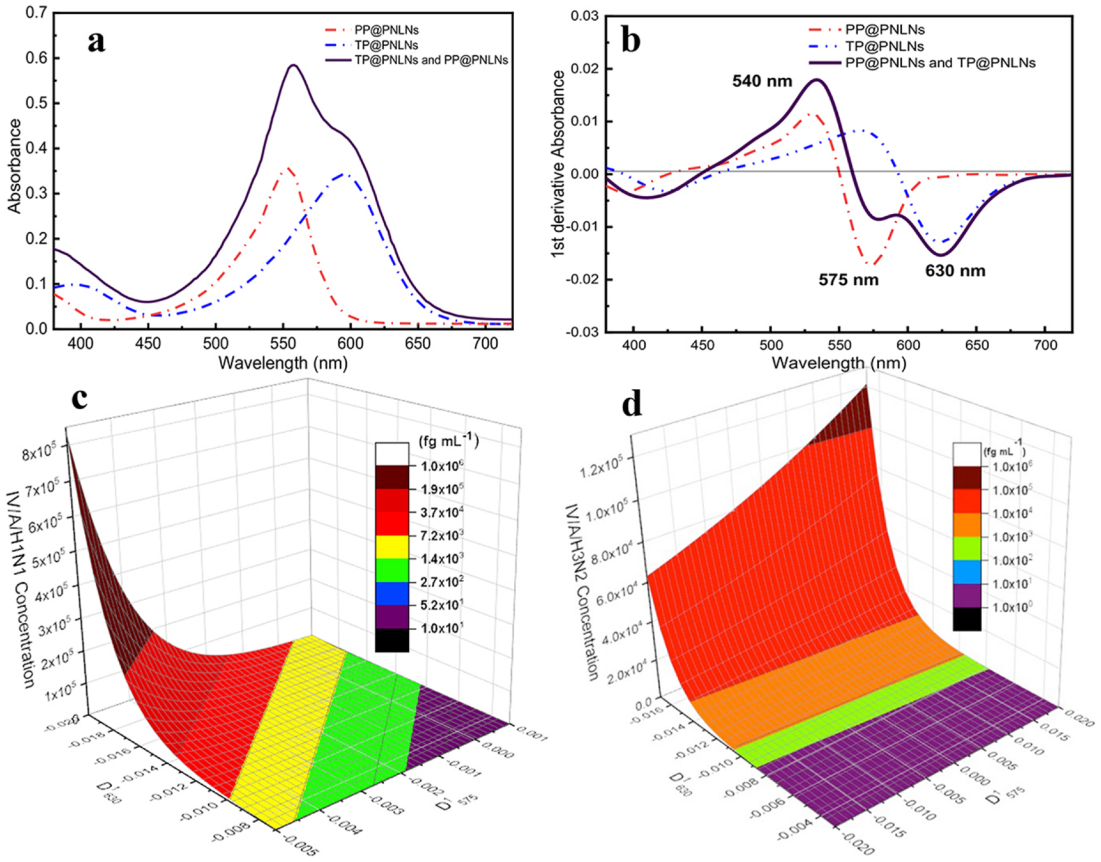

Figure 4. Binary response of the PNLN-based biosensor. (a) Absorbance spectra of PP@PNLNs, TP@PNLNs, and PNLN mixtures. (b) First derivation absorbance spectra of the PNLN mixtures. Simulated derivative binary response model in determining (c) the IV/A/H1N1 concentration and (d) IV/A/H3N2 concentration.

IV/A solution (sample) (Figure 3a-i). After the Ab-MNPs/(IV/A)/(Ab-PP@PNLs or Ab-TP@PNLNs) immunosandwich complex was formed, the magnetic field separated it, and nonbinding PP(TP)@PNLNs were removed from the system (Figure 3a-ii). The separated complex was redispersed and transferred to the reaction chamber containing 1 M NaOH solution (Figure 3a-iii). As the alkaline solution disrupts the polymeric membrane and exposes the chromogen to the hydroxide ions, the color is developed in the well plate. The color develops depending on the amount of chromogen in the bound Ab-PP(TP)@PNLNs in the sandwich complex. As the formation of the sandwich complex can be limited to the number of viruses and the unbound chromogen carrier is washed out, the presence of the virus can be quantified by the developed color.

The initial assessment demonstrates the essential components for the immunosandwich formation of Ab-MNPs, IV/A, and Ab-PP(TP)@PNLNs. IV/A/H1N1 was mixed with only Ab-MNPs, only Ab-PP@PNLNs, or both. As shown in Figure S8 in the Supporting Information, only when Ab-MNPs and Ab-PP@PNLNs were added into the IV/A/H1N1 solution, there is a positive signal, demonstrating the increased absorbance at 550 nm (A_{550}). This shows that each component is essential to isolate the virus specifically and generates the detection signal. Additionally, as shown in Figure S9a, the immunosandwich is roughly visualized by TEM image analysis due to the high contrast of electrons between the MNPs and both the virus and PNLNs. In addition, Figure S9b shows that the immunosandwich structure is not observed after the alkaline solution is added to the nanocomposite.

Next, individually, the PNLNs are initially tested on the corresponding subtype of IV/A. Ab-PP@PNLNs and Ab-TP@PNLNs were tested to detect IV/A/H1N1 and IV/A/H3N2, respectively. The positive result of the detection will develop a pinkish color with the absorbance at 560 nm and a bluish color with the absorbance at 595 nm representing the presence of IV/A/H1N1 and IV/A/H3N2, respectively.

In the PP@PNLNs-based IV/A/H1N1 biosensor, the absorbance spectra were obtained from the IV/A/H1N1 detection from 10^0 to 10^{-6} fg mL^{-1} virus concentration. Figure 3b-i shows that the absorbance at 560 nm increases along the increase in IV/A/H1N1 concentration in the sample. Depending on the virus's increasing concentration, the developed color in the alkaline solution shows a pinkish color, forming a gradient pattern from low to dark pink color. The absorbance at 560 nm (A_{560}) is plotted as a function of IV/A/H1N1 concentration. The calibration line using A_{560} as a function of IV/A/H1N1 concentration is obtained with a correlation coefficient (R^2) of 0.953 and with satisfactory linearity from 10^1 to 10^6 fg mL^{-1} (Figure 3b-ii). Also, the limit of detection (LOD) is 27.56 fg/mL, which is determined by calculating with the equation $3\sigma/S$,[47] in which S and σ represent the slope of the calibration line and the absorbance of the lowest detectable signal, respectively. For the selectivity line, the PP@PNLNs-based biosensor is assayed to several subtypes of influenza viruses, such as IV/A/H3N2, IV/A/H5N1, and IV/A/H9N2, including other virus recombinant proteins, such as

https://doi.org/10.1021/acsami.1c08813
ACS Appl. Mater. Interfaces 2021, 13, 36868−36879

HEV-LPs and NoV-LPs. As the antibodies of the Ab-PP@PNLNs detect the specific surface protein of H1N1, there is no signal corresponding to the other viruses except IV/A/H1N1 (Figure 3b-iii), and the selectivity of the developed biosensor can be achieved. The biosensor indicates a slightly response signal on IV/A/H3N2, which is a consequence of the binding capability of Ab-MNPs to hemagglutinins H1, H2, and H3 of IV/A. However, a slight signal is not adjudged to a high signal of the IV/A/H1N1 detection signal.

Parallel to the IV/A/H1N1 detection, a TP@PNLNs-based biosensor was utilized to detect IV/A/H3N2. The increasing absorbance signal at 595 nm intensified correspondingly to increasing concentration of the IV/A/H3N2 virus from 10^0 to 10^6 fg mL^{-1} (Figure 3c-i). The absorbance value at 595 nm was plotted against the concentration of IV/A/H3N2 in the sample. The linear response of the biosensor with A_{595} as a function of IV/A/H3N2 concentration is performed in decent concentration from 10^1 to 10^6 fg mL^{-1} with R^2 of 0.982 and a detection limit of 28.38 fg mL^{-1} (Figure 3c-ii). The selectivity of the developed TP@PNLNs-based biosensor for IV/A/H3N2 detection was evaluated against different subtypes of IV/A and virus-like particle protein recombinants. The high difference between the absorbance value of the target and nontarget promotes the excellent selectivity of the developed biosensor (Figure 3c-iii), which is contributed by the specific binding of the antibody-conjugated TP@PNLNs to IV/A/H3N2.

Several intrinsic points need to be highlighted owing to the superior performance of the PNLN-based biosensor. (1) Compared to protein-assisted nanoprecipitation,[30] the utilization of the three-solvent system forms the nanoparticle laden with a higher amount of chromogen. The higher-loaded nanocarrier can amplify the signal on individual antibody−antigen binding up to the subfemtogram level. (2) The coreactivity of the polymeric boundary and the dye to the alkaline condition results in fast color development compared to other pH-sensitive biosensing systems.[25,27] (3) The involvement of magnetic separation in the biosensor can enrich the target analytes and forms a higher quantity of immunosandwich structures and shorter incubation time for antibody−antigen conjugation due to its high surface area. The overall system took 15 min, which enables a faster detection time compared to our previously developed biosensor.[48]

Binary Response of the PNLN-Based Biosensor in the Detection of IV/A Subtype. The PNLN-based biosensor is developed to transcend the available immunoassay format regarding its applicability in multiple detections. With the dependency solely on quantifying the substrate's catalytic reaction, the available biosensor is still striving to accommodate the identification function of virus subtypes. By using nanocarriers, which are conjugated to antibodies specific to IV/A, the developed biosensor utilizes PP@PNLNs and TP@PNLNs to generate a binary colorimetric signal depending on the virus subtypes in the target analyte.

Prior to the IV/A subtype detection, the absorbance of the mixture of PNLNs is measured to analyze the blend response of the PNLN-based biosensor. As shown in Figure 4a, the absorbance spectra of the TP@PNLNs and PP@PNLNs were merged and showed two peaks of the absorbance, resulting in a darkish bluish-purple color in the detection chamber. The absorbance spectra of the TP@PNLNs, PP@PNLNs, and PNLN mixtures were transformed into their first derivation absorbance spectra. The derivation absorbance indicates the change in absorbance in an interval of wavelength, which deconvolutes the merged peak into multiple inflection points, indicating the target signals.[49,50] Figure 4b shows the first derivation absorbance of the PNLN mixtures. There are three inflection regions of interest in the derivative spectra: absorbances at 540, 575, and 630 nm. The absorbances of both PNLNs are overlapping each other at a wavelength of 540 nm.

On the other hand, the absorbance of TP@PNLNs dominates the absorbance at 630 nm. Interestingly, the absorbance at 575 nm is contributed by PNLNs with PP@PNLNs moving the absorbance to a positive value and TP@PNLNs moving the absorbance to a negative value. As a non-overlapping signal in the PNLN mixture signal, the first derivation absorbances at 575 and 630 nm are determined as the binary signal of the PNLN-based biosensor.

To construct a one-step and single readout detection purpose, both PP@PNLNs and TP@PNLNs were co-added in the PNLN-based biosensor. The biosensor was applied to detect IV/A/H1N1 (Figure S7a) and IV/A/H3N2 (Figure S7b) in the range of 10^1 to 10^5 fg mL^{-1}. To understand the contribution of each PNLN on the binary response of the developed biosensor, the first derivation absorbances of IV/A/H1N1 and IV/A/H3N2 detection at 575 and 630 nm were plotted against the concentration of the corresponding IV/A. The slope of the calibration line of the absorbance signal vs the IV/A concentration represented the contribution factor (CF) of the PP@PNLNs and TP@PNLNs on the binary response of the PNLN-based biosensor. As shown in Figure S7c, the developed biosensor exhibits different signal patterns according to the subtype of IV/A with a negative slope for IV/A/H1N1 and a positive slope for IV/A/H3N2. The CF values of the PP@PNLNs and TP@PNLNs for the absorbance at 575 nm are -2.55×10^{-3} and $+1.67 \times 10^{-3}$, respectively. Figure S7d shows the plot of the first derivate absorbance at 630 nm as the function of IV/A concentration. It unveils clearly that there is a low signal of IV/A/H1N1 detection in this region compared to IV/A/H3N2 detection. It is as expected as PP@PNLNs do not exhibit a signal up to the absorbance region at 630 nm. As it is solely contributed by TP@PNLNs, the CF values of PNLNs at the first derivative absorbance at 630 nm are $+6.02 \times 10^{-5}$ for PP@PNLNs and -3.20×10^{-3} for TP@PNLNs. Hence, the overall equation of the binary response of the PNLN-based biosensor can be expressed as

$$D^1_{575} = -2.55 \times 10^{-3} \log(C_{H1N1}) + 1.67 \times 10^{-3} \log(C_{H3N2}) \quad (1)$$

$$D^1_{630} = +6.02 \times 10^{-5} \log(C_{H1N1}) - 3.20 \times 10^{-3} \log(C_{H3N2}) \quad (2)$$

with binary responses of the PNLN-based biosensor as D^1_{575} and D^1_{630} representing the first derivate absorbances at 575 and 630 nm, respectively; C_{H1N1} and C_{H3N2} represent the IV/A/H1N1 and IV/A/H3N2 concentrations, respectively.

Accordingly, eqs 1 and 2 are rearranged by the coefficient elimination method to be able to determine the IV/A/H1N1 concentration and IV/A/H3N2 concentration depending upon the value of the D^1_{575} and D^1_{630}. The concentration of IV/A can be expressed as:

$$C_{H1N1} = 10^{(-3.20\times10^{-3}D^1_{575} - 1.67\times10^{-3}D^1_{630})/8.26\times10^{-6}} \quad (3)$$

https://doi.org/10.1021/acsami.1c08813
ACS Appl. Mater. Interfaces 2021, 13, 36868−36879

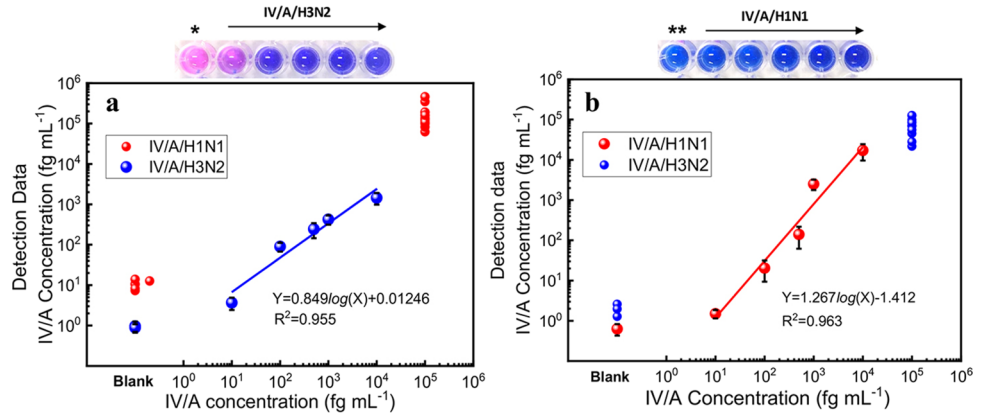

Figure 5. Binary detection of IV/A/H1N1 and IV/A/H3N2 in IV/A solutions by the PNLN-based biosensor. Panel (a) represents the detected concentration of IV/A/H1N1 (red circle) and IV/A/H3N2 (blue circle) in mixture set A; panel (b) represents the detected concentration of IV/A/H3N2 (blue circle) and IV/A/H1N1 (red circle) in mixture set B. Mixture set A contains a fixed concentration of 10^5 fg mL^{-1} IV/A/H1N1 and a series concentration of IV/A/H3N2 from 10^1 to 10^4 fg mL^{-1} (0, 10, 100, 500, 1000, and 10,000 fg mL^{-1}); mixture set B contains a fixed concentration of 10^5 fg mL^{-1} IV/A/H3N2 and a series concentration of IV/A/H1N1 from 10^1 to 10^4 fg mL^{-1} (0, 10, 100, 500, 1000, and 10,000 fg mL^{-1}). The digital image shows the developed color taken by a smartphone camera. (The single asterisk (*) indicates the detection of only IV/A/H1N1, and the double asterisk (**) indicates the detection of only IV/A/H3N2. Both serve as the positive control in the binary detection.)

$$C_{H3N2} = 10^{(6.02\times10^{-5}D^1_{575}+2.55\times10^{-3}D^1_{630})/8.26\times10^{-6}} \quad (4)$$

Based on eqs 3 and 4, the ranges of D^1_{575} and D^1_{630} are plotted in the matrix calculation to simulate the detected IV/A/H1N1 concentration. Figure 4c shows the pattern of the IV/A/H1N1 concentration at the limit range from −0.005 to +0.001 for D^1_{575} and −0.007 to −0.02 for D^1_{630}. The concentration obtained has a range with a minimum value of 10^0 fg mL^{-1} and a maximum value of 10^6 fg mL^{-1}. The pattern indicates that the maximal concentration of IV/A/H1N1 is toward the $-D^1_{575}$ and $-D^1_{630}$. On the other side, Figure 4d shows the plot of IV/A/H3N2 as the function of D^1_{575} and D^1_{630}. The ranges of the D^1_{575} and D^1_{630} are determined as −0.02 to +0.02 and −0.004 to −0.016, respectively. The pattern demonstrates that the shifting value of D^1_{630} could determine the range of the IV/A/H3N2 concentration as the window of the concentration scale upon which the D^1_{575} is wider than the window scale of D^1_{630}. Overall, the derivative binary response of the biosensor can be utilized to determine the concentration of IV/A/H1N1 and IV/A/H3N2 based on the coefficient factors of PP@PNLNs and TP@PNLNs as the parameters.

Binary Detection of the Subtype IV/A Detection. The binary detection performance of the PNLN-based biosensor is carried out in the mixtures of subtype IV/A solutions (Scheme S1), which are denoted as mixture set A and mixture set B. Mixture set A contains a series concentration of IV/A/H3N2 from 10^1 to 10^4 fg mL^{-1} at a fixed concentration of 10^5 fg mL^{-1} IV/A/H1N1. Mixture set B has a series concentration of IV/A/H1N1 from 10^1 to 10^4 fg mL^{-1} at a fixed concentration of 10^5 fg mL^{-1} IV/A/H3N2. Figure S10a displays the PNLN-based biosensor performance in mixture set A detection. The absorbance shows a sole peak at 575 nm in a negative value of -1.2×10^{-3} as there is only IV/A/H1N1 in the solution. As the concentration of IV/A/H3N2 is gradually increasing, the peak absorbance at 575 nm is gradually decreasing, and the absorbance at 630 nm increases corresponding to the increasing concentration of IV/A/H3N2 (Figure S10c). Similarly, Figure S10b shows that the PNLN-based biosensor was applied to mixture set B. In the presence of only IV/A/H3N2 in mixture set B, the derivative absorbances at 575 and 630 nm are 5.98×10^{-3} and -1.38×10^{-2}, respectively. The gradual movement of the first derivative absorbance at 575 nm from the positive value to a negative value corresponds to the higher concentration of IV/A/H1N1 in mixture set B (Figure S10d).

To evaluate the binary detection performance by the PNLN-based biosensor, the binary responses (eqs 1 and 2) of the developed biosensor were used to determine the detected concentration of IV/A/H1N1 and IV/A/H3N2 in mixture sets A and B based on the derivative absorbance spectra (Figure S11). Figure 5a displays the detection performance of the PNLN-based biosensor in mixture set A. Simultaneously, the obtained concentration of IV/A/H1N1 in mixture set A is around $(1.58 \pm 0.33) \times 10^5$ fg mL^{-1} IV/A/H1N1 and a linear response corresponds to the concentration of IV/A/H3N2 in mixture set A starting from 10^1 to 10^4 fg mL^{-1} with R^2 of 0.955. Figure 5b shows the detection of IV/A/H1N1 and IV/A/H3N2 in mixture set B. The PNLN-based biosensor indicates detection of $(7.23 \pm 1.27) \times 10^4$ fg mL^{-1} IV/A/H3N2 with a variance coefficient around 25.8% and an excellent linear response from 10^1 to 10^4 fg mL^{-1} IV/A/H1N1 detection in mixture set B with R^2 of 0.963. Overall, the PNLN-based biosensor demonstrates multiple detection of the IV/A subtype in a single readout with a cutoff background signal up to 13.9 fg mL^{-1} based on the blank sample detection. Furthermore, based on the linearity of the log−log plot of the detected virus concentration vs IV/A concentration determined by ELISA, there are an overestimation to 18.6% for IV/A/H1N1 detection and underestimation down to 15.1% for IV/A/H3N2 detection.

Further investigation evaluates the performance of the PNLN-based biosensor for subtype detection of IV/A in human serum. As shown in Table S1, the detection shows 86.1−124.8% recovery in concentrated 10% human serum and 93.5−110.67% recovery in diluted 2% human serum. Because of the Ab-MNPs and magnetic separation, matrix solutions such as human serum have a minimum effect on detecting the influenza virus by the PNLN-based biosensor. The major factor of drawback in the PNLN-based biosensor is possibly due to the competitive binding of IV/A/H3N2 and IV/A/H1N1, forming an immunosandwich structure in the mixture

https://doi.org/10.1021/acsami.1c08813
ACS Appl. Mater. Interfaces 2021, 13, 36868−36879

virus solution, and the difference in the dissociation constant of both chromogens.

The derivative binary response of the PNLN-based biosensor shows a feasible approach for subtype detection of the influenza virus. By applying the one-pot detection, starting from the immunoassay to the sensing step, the developed biosensor substantiates the simplicity of the dual-targeting virus detection, which does not require complex platform fabrication[15] or complex signal analysis.[6,31] Further, compared to the presently developed biosensor (Table S2), the developed biosensor using PNLNs keeps its sensitivity in the subfemtogram level for the simultaneous binary IV/A subtype detection. Although the developed binary response biosensor could not guarantee the advancement in signal amplification, it is able to enrich the selectiveness of the virus detection platform. Several factors impede the further scale of this biosensor, including the limited variety of the chromogen in a similar range of stimuli and the physicochemical properties, such as solubility and colloidal stability. Further studies with multiple polymers are recommended to show the performance of the PNLNs in the biosensor.

CONCLUSIONS

This work describes the high loading of pH-sensitive PNLNs for specific virus detection in the mixture of subtypes of the influenza virus by the binary response of the detection signal. The loading of the chromogens, PP and TP, into the PNLNs can be influenced by the types of solvents and their intrinsic properties. The higher loading capacity PNLNs show higher signal amplification in the detection sensitivity with the LODs of IV/A/H1N1 and IV/A/H3N2 of 27.56 and 28.38 fg mL^{-1}, respectively. The developed biosensor shows a binary response of the PNLNs in the detection of virus subtypes in the detection readout. The PNLN-based biosensor successfully detected IV/A/H1N1 with an overestimation of 18.6% and IV/A/H3N2 with 15.1% underestimation. The coefficient of variance is calculated at 21.5% based on the subtype IV/A detection. Hence, binary detection of IV/A in a single readout has been fabricated based on the chromogens and nanocarriers, which will open-up two-dimensional identification of the virus sensing.

ASSOCIATED CONTENT

Supporting Information

The Supporting Information is available free of charge at https://pubs.acs.org/doi/10.1021/acsami.1c08813.

Table S1: recovery test of the binary detection of IV/A/H1N1 and IV/A/H3N2 in human serum using the PNLN-based biosensor; Table S2: comparison of the present biosensor technique for IV/A detection; Scheme S1: illustration for binary IV/A detection using Ab-PNLNs and Ab-MNPs; Figure S1: PP@PNLs in a three-solvent mixture with chromogen/polymer (2:1, v/v); Figure S2: hydrodynamic size and PDI of phenolphthalein in a one-solvent system; Figure S3: TEM image of TP@PNLNs; Figure S4: concentration dependence of phenolphthalein (PP) vs absorbance; Figure S5: ELISA confirmation of the antibody conjugation to PNLNs and MNPs; Figure S6: influenza virus detection using the Ab-PP@PNLNs-based biosensor; Figure S7: characteristic of amine-functionalized magnetic nanoparticles (A-MNPs); Figure S8: detection of IV/A/H1N1 by varying combinations of IV/A/H1N1, Ab-MNPs, and Ab-PP@PNLNs; Figure S9: TEM image of the immunosandwich formation; Figure S10: contribution factor of PP@PNLNs and TP@PNLNs in the binary response of the developed biosensor; Figure S11: first derivative absorbance spectra of binary detection on IV/A by the PNLN-based biosensor (PDF)

AUTHOR INFORMATION

Corresponding Author

Enoch Y. Park − *Department of Bioscience, Graduate School of Science and Technology and Research Institute of Green Science and Technology, Shizuoka University, Shizuoka 422-8529, Japan*; orcid.org/0000-0002-7840-1424; Email: park.enoch@shizuoka.ac.jp

Authors

Indra Memdi Khoris − *Department of Bioscience, Graduate School of Science and Technology, Shizuoka University, Shizuoka 422-8529, Japan*

Akhilesh Babu Ganganboina − *Research Institute of Green Science and Technology, Shizuoka University, Shizuoka 422-8529, Japan*

Complete contact information is available at: https://pubs.acs.org/10.1021/acsami.1c08813

Author Contributions

I.M.K. and A.B.G. conceived the idea behind this work. I.M.K. performed the methodology development and acquired data. I.M.K. and A.B.G. analyzed the experimental results and wrote the manuscript. A.B.G. and E.Y.P. reviewed and revised the manuscript. E.Y.P. supervised the work. All authors have given approval to the final version of the manuscript.

Notes

The authors declare no competing financial interest.

ACKNOWLEDGMENTS

We would like to express our sincere gratitude to Dr. T. C. Li of National Institute of Infectious Diseases for providing HEV-LPs for the selectivity test. A.B.G. and I.M.K. sincerely thank the Japan Society for the Promotion of Science (JSPS) for a postdoctoral fellowship (19F19064) and research fellowship DC (20J22358), respectively. E.Y.P. sincerely thanks the Japan Agency for Medical Research and Development (20hm0102080h0001).

REFERENCES

(1) Petersen, E.; Koopmans, M.; Go, U.; Hamer, D. H.; Petrosillo, N.; Castelli, F.; Storgaard, M.; Al Khalili, S.; Simonsen, L. Comparing SARS-CoV-2 with SARS-CoV and Influenza Pandemics. *Lancet Infect. Dis.* **2020**, *20*, e238−e244.

(2) Zhang, H.; Miller, B. L. Immunosensor-Based Label-Free and Multiplex Detection of Influenza Viruses: State of the Art. *Biosens. Bioelectron.* **2019**, *141*, 111476.

(3) Dahmana, H.; Mediannikov, O. Mosquito-Borne Diseases Emergence/Resurgence and How to Effectively Control It Biologically. *Pathogens* **2020**, *9*, 310.

(4) Ganganboina, A. B.; Khoris, I. M.; Chowdhury, A. D.; Li, T.-C.; Park, E. Y. Ultrasensitive Detection of the Hepatitis E Virus by Electrocatalytic Water Oxidation Using Pt-Co_3O_4 Hollow Cages. *ACS Appl. Mater. Interfaces* **2020**, *12*, 50212−50221.

(5) Dang, V. D.; Ganganboina, A. B.; Doong, R.-A. Bipyridine-and Copper-Functionalized N-Doped Carbon Dots for Fluorescence Turn

Off−On Detection of Ciprofloxacin. *ACS Appl. Mater. Interfaces* **2020**, *12*, 32247−32258.
(6) Wu, Z.; Zeng, T.; Guo, W.-J.; Bai, Y.-Y.; Pang, D.-W.; Zhang, Z.-L. Digital Single Virus Immunoassay for Ultrasensitive Multiplex Avian Influenza Virus Detection Based on Fluorescent Magnetic Multifunctional Nanospheres. *ACS Appl. Mater. Interfaces* **2019**, *11*, 5762−5770.
(7) Suzuki, A.; Mizumoto, K.; Akhmetzhanov, A. R.; Nishiura, H. Interaction among Influenza Viruses A/H1N1, A/H3N2, and B in Japan. *Int. J. Environ. Res. Public Health* **2019**, *16*, 4179.
(8) Ison, M. G. Antivirals and Resistance: Influenza Virus. *Curr. Opin. Virol.* **2011**, *1*, 563−573.
(9) Lampejo, T. Influenza and Antiviral Resistance: An Overview. *Eur. J. Clin. Microbiol. Infect. Dis.* **2020**, *39*, 1201−1208.
(10) Ganganboina, A. B.; Chowdhury, A. D.; Khoris, I. M.; Doong, R.-a.; Li, T.-C.; Hara, T.; Abe, F.; Suzuki, T.; Park, E. Y. Hollow Magnetic-Fluorescent Nanoparticles for Dual-Modality Virus Detection. *Biosens. Bioelectron.* **2020**, *170*, 112680.
(11) Oh, S.; Kim, J.; Tran, V. T.; Lee, D. K.; Ahmed, S. R.; Hong, J. C.; Lee, J.; Park, E. Y.; Lee, J. Magnetic Nanozyme-Linked Immunosorbent Assay for Ultrasensitive Influenza A Virus Detection. *ACS Appl. Mater. Interfaces* **2018**, *10*, 12534−12543.
(12) Takemura, K.; Adegoke, O.; Takahashi, N.; Kato, T.; Li, T.-C.; Kitamoto, N.; Tanaka, T.; Suzuki, T.; Park, E. Y. Versatility of a Localized Surface Plasmon Resonance-Based Gold Nanoparticle-Alloyed Quantum Dot Nanobiosensor for Immunofluorescence Detection of Viruses. *Biosens. Bioelectron.* **2017**, *89*, 998−1005.
(13) Wang, C.; Gao, J.; Tan, H. Integrated Antibody with Catalytic Metal−Organic Framework for Colorimetric Immunoassay. *ACS Appl. Mater. Interfaces* **2018**, *10*, 25113−25120.
(14) Bhardwaj, J.; Chaudhary, N.; Kim, H.; Jang, J. Subtyping of Influenza a H1N1 Virus Using a Label-Free Electrochemical Biosensor Based on the DNA Aptamer Targeting the Stem Region of HA Protein. *Anal. Chim. Acta* **2019**, *1064*, 94−103.
(15) Yao, Y.; Chen, X.; Zhang, X.; Liu, Q.; Zhu, J.; Zhao, W.; Liu, S.; Sui, G. Rapid Detection of Influenza Virus Subtypes Based on an Integrated Centrifugal Disc. *ACS Sens.* **2020**, *5*, 1354−1362.
(16) Duchamp, M. B.; Casalegno, J.; Gillet, Y.; Frobert, E.; Bernard, E.; Escuret, V.; Billaud, G.; Valette, M.; Javouhey, E.; Lina, B. Pandemic a (H1N1) 2009 Influenza Virus Detection by Real Time RT-PCR: Is Viral Quantification Useful? *Clin. Microbiol. Infect.* **2010**, *16*, 317−321.
(17) Arima, A.; Tsutsui, M.; Yoshida, T.; Tatematsu, K.; Yamazaki, T.; Yokota, K.; Kuroda, S.; Washio, T.; Baba, Y.; Kawai, T. Digital Pathology Platform for Respiratory Tract Infection Diagnosis Via Multiplex Single-Particle Detections. *ACS Sens.* **2020**, *5*, 3398−3403.
(18) Laconi, A.; Fortin, A.; Bedendo, G.; Shibata, A.; Sakoda, Y.; Awuni, J. A.; Go-Maro, E.; Arafa, A.; Ali, A. S. M.; Terregino, C. Detection of Avian Influenza Virus: A Comparative Study of the in Silico and in Vitro Performances of Current RT-qPCR Assays. *Sci. Rep.* **2020**, *10*, 8441.
(19) Xu, S.; Ouyang, W.; Xie, P.; Lin, Y.; Qiu, B.; Lin, Z.; Chen, G.; Guo, L. Highly Uniform Gold Nanobipyramids for Ultrasensitive Colorimetric Detection of Influenza Virus. *Anal. Chem.* **2017**, *89*, 1617−1623.
(20) Khoris, I. M.; Takemura, K.; Lee, J.; Hara, T.; Abe, F.; Suzuki, T.; Park, E. Y. Enhanced Colorimetric Detection of Norovirus Using in-situ Growth of Ag Shell on Au NPs. *Biosens. Bioelectron.* **2019**, *126*, 425−432.
(21) Wang, R.; Ongagna-Yhombi, S. Y.; Lu, Z.; Centeno-Tablante, E.; Colt, S.; Cao, X.; Ren, Y.; Cárdenas, W. B.; Mehta, S.; Erickson, D. Rapid Diagnostic Platform for Colorimetric Differential Detection of Dengue and Chikungunya Viral Infections. *Anal. Chem.* **2019**, *91*, 5415−5423.
(22) Zhu, L.; Liu, X.; Yang, J.; He, Y.; Li, Y. Application of Multiplex Microfluidic Electrochemical Sensors in Monitoring Hematological Tumor Biomarkers. *Anal. Chem.* **2020**, *92*, 11981−11986.
(23) Li, Z.; Zhang, S.; Yu, T.; Dai, Z.; Wei, Q. Aptamer-Based Fluorescent Sensor Array for Multiplexed Detection of Cyanotoxins on a Smartphone. *Anal. Chem.* **2019**, *91*, 10448−10457.
(24) Miao, L.; Zhu, C.; Jiao, L.; Li, H.; Du, D.; Lin, Y.; Wei, Q. Smart Drug Delivery System-Inspired Enzyme-Linked Immunosorbent Assay Based on Fluorescence Resonance Energy Transfer and Allochroic Effect Induced Dual-Modal Colorimetric and Fluorescent Detection. *Anal. Chem.* **2018**, *90*, 1976−1982.
(25) Ren, R.; Cai, G.; Yu, Z.; Zeng, Y.; Tang, D. Metal-Polydopamine Framework: An Innovative Signal-Generation Tag for Colorimetric Immunoassay. *Anal. Chem.* **2018**, *90*, 11099−11105.
(26) Shen, S.; Wu, Y.; Liu, Y.; Wu, D. High Drug-Loading Nanomedicines: Progress, Current Status, and Prospects. *Int. J. Nanomed.* **2017**, *Volume 12*, 4085.
(27) Yan, H.; Jiao, L.; Wang, H.; Xu, W.; Wu, Y.; Gu, W.; Du, D.; Lin, Y.; Zhu, C. A "Sense-and-Treat" Elisa Using Zeolitic Imidazolate Framework-8 as Carriers for Dual-Modal Detection of Carcinoembryonic Antigen. *Sens. Actuators, B* **2019**, *297*, 126760.
(28) Sun, Y.; Zheng, L.; Yang, Y.; Qian, X.; Fu, T.; Li, X.; Yang, Z.; Yan, H.; Cui, C.; Tan, W. Metal−Organic Framework Nanocarriers for Drug Delivery in Biomedical Applications. *Nano Micro. Lett.* **2020**, *12*, 103.
(29) Liu, Y.; Yang, G.; Baby, T.; Chen, D.; Weitz, D. A.; Zhao, C. X. Stable Polymer Nanoparticles with Exceptionally High Drug Loading by Sequential Nanoprecipitation. *Angew. Chem., Int. Ed.* **2020**, *59*, 4720−4728.
(30) Xu, W.; Jiao, L.; Ye, H.; Guo, Z.; Wu, Y.; Yan, H.; Gu, W.; Du, D.; Lin, Y.; Zhu, C. Ph-Responsive Allochroic Nanoparticles for the Multicolor Detection of Breast Cancer Biomarkers. *Biosens. Bioelectron.* **2020**, *148*, 111780.
(31) Wu, K.; Liu, J.; Saha, R.; Su, D.; Krishna, V. D.; Cheeran, M. C.-J.; Wang, J.-P. Magnetic Particle Spectroscopy for Detection of Influenza a Virus Subtype H1N1. *ACS Appl. Mater. Interfaces* **2020**, *12*, 13686−13697.
(32) Venkataramanan, N. S. Cooperativity of Intermolecular Hydrogen Bonds in Microsolvated DMSO and DMF Clusters: A DFT, AIM, and NCI Analysis. *J. Mol. Model.* **2016**, *22*, 151.
(33) Bilati, U.; Allémann, E.; Doelker, E. Development of a Nanoprecipitation Method Intended for the Entrapment of Hydrophilic Drugs into Nanoparticles. *Eur. J. Pharm. Sci.* **2005**, *24*, 67−75.
(34) Ahmed, S. R.; Takemeura, K.; Li, T.-C.; Kitamoto, N.; Tanaka, T.; Suzuki, T.; Park, E. Y. Size-Controlled Preparation of Peroxidase-Like Graphene-Gold Nanoparticle Hybrids for the Visible Detection of Norovirus-Like Particles. *Biosens. Bioelectron.* **2017**, *87*, 558−565.
(35) Robinson, D. A.; Stevenson, K. J. Uniform Epitaxial Growth of Pt on Fe_3O_4 Nanoparticles; Synergetic Enhancement to Pt Activity for the Oxygen Reduction Reaction. *J. Mater. Chem. A* **2013**, *1*, 13443−13453.
(36) Ganganboina, A. B.; Chowdhury, A. D.; Khoris, I. M.; Nasrin, F.; Takemura, K.; Hara, T.; Abe, F.; Suzuki, T.; Park, E. Y. Dual Modality Sensor Using Liposome-Based Signal Amplification Technique for Ultrasensitive Norovirus Detection. *Biosens. Bioelectron.* **2020**, 112169.
(37) Leong, S. S.; Ng, W. M.; Lim, J.; Yeap, S. P., Dynamic Light Scattering: Effective Sizing Technique for Characterization of Magnetic Nanoparticles. In *Handbook of Materials Characterization*, Springer: 2018; pp. 77−111, DOI: 10.1007/978-3-319-92955-2_3.
(38) Shang, J.; Gao, X. Nanoparticle Counting: Towards Accurate Determination of the Molar Concentration. *Chem. Soc. Rev.* **2014**, *43*, 7267−7278.
(39) Vysotskii, V. V.; Uryupina, O. Y.; Gusel'nikova, A.; Roldugin, V. I. On the Feasibility of Determining Nanoparticle Concentration by the Dynamic Light Scattering Method. *Colloid J.* **2009**, *71*, 739.
(40) Andrews, J.; Blaisten-Barojas, E. Exploring with Molecular Dynamics the Structural Fate of PLGA Oligomers in Various Solvents. *J. Phys. Chem. B* **2019**, *123*, 10233−10244.
(41) Wilkosz, N.; Łazarski, G.; Kovacik, L.; Gargas, P.; Nowakowska, M.; Jamróz, D.; Kepczynski, M. Molecular Insight into Drug-Loading

Capacity of PEG−PLGA Nanoparticles for Itraconazole. *J. Phys. Chem. B* **2018**, *122*, 7080−7090.
(42) Fedors, R. F. A Method for Estimating Both the Solubility Parameters and Molar Volumes of Liquids. *Polym. Eng. Sci.* **1974**, *14*, 147−154.
(43) Figueroa, S. M.; Fleischmann, D.; Beck, S.; Goepferich, A. Thermodynamic, Spatial and Methodological Considerations for the Manufacturing of Therapeutic Polymer Nanoparticles. *Pharm. Res.* **2020**, *37*, 59.
(44) Li, J.; Stayshich, R. M.; Meyer, T. Y. Exploiting Sequence to Control the Hydrolysis Behavior of Biodegradable PLGA Copolymers. *J. Am. Chem. Soc.* **2011**, *133*, 6910−6913.
(45) Gulzar, A.; Gai, S.; Yang, P.; Li, C.; Ansari, M. B.; Lin, J. Stimuli Responsive Drug Delivery Application of Polymer and Silica in Biomedicine. *J. Mater. Chem. B* **2015**, *3*, 8599−8622.
(46) Chen, Y.; Xianyu, Y.; Wang, Y.; Zhang, X.; Cha, R.; Sun, J.; Jiang, X. One-Step Detection of Pathogens and Viruses: Combining Magnetic Relaxation Switching and Magnetic Separation. *ACS Nano* **2015**, *9*, 3184−3191.
(47) Ganganboina, A. B.; Doong, R.-A. Graphene Quantum Dots Decorated Gold-Polyaniline Nanowire for Impedimetric Detection of Carcinoembryonic Antigen. *Sci. Rep.* **2019**, *9*, 7214.
(48) Khoris, I. M.; Ganganboina, A. B.; Suzuki, T.; Park, E. Y. Self-Assembled Chromogen-Loaded Polymeric Cocoon for Respiratory Virus Detection. *Nanoscale* **2021**, *13*, 388−396.
(49) Shams Nateri, A.; Ekrami, E. Determination of Bicomponent Dye Solutions by Means of Zero-Crossing-Point Derivative Spectrophotometry. *Color Res. Appl.* **2008**, *33*, 307−311.
(50) Li, Y.; Wang, S.; Shen, Z.; Li, X.; Zhou, Q.; Sun, Y.; Wang, T.; Liu, Y.; Gao, Q. Gradient Adsorption of Methylene Blue and Crystal Violet onto Compound Microporous Silica from Aqueous Medium. *ACS Omega* **2020**, *5*, 28382−28392.

https://doi.org/10.1021/acsami.1c08813
ACS Appl. Mater. Interfaces 2021, 13, 36868−36879